JOURNAL OF CATALYSIS 144, 254–272 (1993)

Heterogeneities in Structure and Diffusion within Porous Catalyst Support Pellets Observed by NMR Imaging

MICHAEL P. HOLLEWAND AND LYNN F. GLADDEN

Department of Chemical Engineering, University of Cambridge, Pembroke Street, Cambridge CB2 3RA, United Kingdom

Received March 24, 1993; revised June 4, 1993

The pore structure of porous oxide pellets commonly used as catalyst supports or as adsorbents in separation processes continues to attract much attention. This paper presents the results of a nuclear magnetic resonance (NMR) imaging study of various alumina and silica pellets. Both spin-echo and gradient-reversal techniques have been employed to produce two-dimensional maps of the spin density, spin–lattice relaxation time, and self-diffusion coefficient in the samples. NMR images show that the porous pellets contain significant structural heterogeneity, and this is reflected in the spatially resolved liquid-phase diffusion coefficients. The work suggests that NMR imaging techniques provide additional information which may be used to complement existing porosimetry and adsorption methods in characterising pore structures. These data will aid in the development of more realistic models of porous solids, which may then be used to predict transport phenomena. The advantage of NMR imaging methods is that they allow the characterisation of pore structure and transport processes within the same experimental environment. The NMR images presented in this paper represent the first application of this technique to visualize the internal structure of and diffusion within porous catalyst support pellets.

INTRODUCTION

For a particular catalytic or adsorption process, the relationships between the pore structure of a supported porous catalyst and the transport phenomena occurring therein are only poorly understood. Because of the complicated nature of porous support materials, the representation of these structures is usually in terms of simplified models; these are reviewed by Sahimi *et al.* (*1*). Typically, the pore structure is considered as comprising a network of voids or pores with a distribution of sizes and an idealised shape; for example, cylinders. While pore connectivity (coordination), pore-size distribution, and pore network topology have all been shown to influence the network conductivity (*2*, *3*), and therefore the catalyst effectiveness under conditions where diffusional controls are important, very little consideration has been given to the existence and effect of heterogeneity on a scale much larger than the pore size. The effects of spatial variations in catalyst activity have been considered from the point of view of tailored profiles of the catalytically active material which have been shown to influence both catalyst selectivity and lifetime (*4*, *5*).

Nuclear magnetic resonance (NMR) spectroscopy is well established as a tool in catalysis. Recently, NMR imaging, originally developed in biomedicine (*6*), has been applied more generally in various applications in materials science (*7*). Solids typically have NMR linewidths of the order 10^4 Hz which are too broad for conventional imaging pulse sequences, and so porous materials are usually imaged by impregnating the material with a liquid phase. An early application of this approach to the imaging of nonbiological samples was a study of moisture in porous building materials (*8*). Later, Rothwell and Vinegar (*9*) imaged a number of brine-soaked oil-field sandstones: maps of the material porosity were obtained by acquiring a series of T_2-

0021-9517/93 $5.00

weighted images. These materials had void sizes of order 1–100 μm and significant spatial variations in the porosity were measured. Much of the research in this field has been motivated by the petroleum industry and as a result many workers have imaged oil and water phases within rock cores. NMR imaging has the advantage over scattering techniques in that the rock matrix is not imaged; however, the presence of paramagnetic impurities in the rock matrix will strongly influence the relaxation properties of the oil and water contained within it, and can in some circumstances make the imaging experiment unviable. Discrimination between oil and water phases is achieved either by relaxation contrast, i.e., exploiting the difference in relaxation time between the two phases (*10*), or by using chemical shift imaging techniques (*11–13*).

NMR imaging studies of fluids in porous solids are not dedicated solely to oil-recovery-based problems. There is much interest in fundamental studies of the structure of porous media and, more recently, the interrelationship between pore structure and transport phenomena. Two recent studies have explored the use of NMR imaging in order to elucidate structural characteristics of porous materials. In the first, Sarkar *et al.* (*14*) studied model porous systems comprising a range of sintered glass discs with pore-sizes from 5–200 μm. In the case of the largest pore-size sample, they found that spin-echo and gradient-reversal imaging sequences produced very different results. This was explained in terms of the magnification of susceptibility boundaries, which arise at the solid–liquid interfaces within the pores, when using the gradient-reversal approach. No comparison was reported for the smaller pore sizes. This effect was also observed by Chang and Komoroski in Ref. (*15*), where defects within elastomers were magnified in the gradient-reversal experiments. The second study (*16, 17*) examined a porous alumina, a sandstone, and a limestone. In the case of the naturally occurring materials significant heterogeneity in spin density was observed; however, the alumina was more homogeneous. Spin density and T_1 images of partially dried samples showed clearly that drying had occurred around the periphery of the samples.

NMR imaging has been used in a number of studies of mass transport in porous solids, initial interest being in polymeric materials. Examples include the high-temperature ingress of water into various epoxy resins (*18*), the determination of the concentration dependence of the diffusion coefficient of water in nylon (*19*), and the diffusion of methanol into polymethylmethacrylate (*20*). More recently, studies of transport in inorganic porous media have been reported. Majors *et al.* (*21*) have measured the effective diffusivity of H_2O–D_2O diffusive exchange in porous alumina. They employed a rapid imaging sequence, and the resulting radially averaged concentration profiles were fitted to the diffusion equation for cylindrical geometries. An alternative approach to studying transport in porous media is to incorporate a PGSE (pulsed-gradient spin-echo) sequence into the imaging experiment. PGSE experiments allow the measurement of self-diffusion without the need for isotopic tracers and their use in catalysis is well-documented, particularly in the case of hydrocarbon transport in zeolites (*22*). Combination of an appropriate PGSE and imaging sequence, first proposed by Redpath *et al.* (*23*), allows the investigator to obtain a map of the spatial variation of the diffusion coefficient. Callaghan and Xia (*24*) have used this approach to obtain images of laminar flow in capillaries, and further experiments have studied the flow of water in plant stems (*25*) and wheat grains (*26*). NMR imaging has also been used by Smith *et al.* (*27*) with the intention of resolving pore-size distributions in sol–gel materials and following changes in structure during the drying of the gel.

This paper extends a preliminary report of NMR imaging of a liquid phase within catalyst pellets (*28*) in which significant het-

erogeneity in the porosity of catalyst supports was observed. This work also forms part of a larger study in which transient diffusion (*29, 30*) and drying phenomena in these systems (*29, 31*) have been studied. The results presented in this paper include the first reported NMR images of spin density, relaxation times, and liquid diffusivity in catalyst support pellets. The experimental difficulties in making these measurements arise from the small sample size and the short T_2^* characteristics of these materials which are inherently associated with microporosity and the nature of the oxide material itself. The results are of interest for two reasons. First, they offer a unique way of both characterising a porous solid and investigating transport phenomena within the material under identical conditions. These data enable a critical analysis of the validity of existing theoretical representations of porous media, and may be used in the development of future numerical modelling schemes. Second, from a commercial point of view, this approach enables a quantitative investigation of the influence of processing parameters on structural heterogeneity. This may be of value if the aim of a particular manufacturing process is to produce pellets with either a high degree of structural uniformity or, conversely, with a controlled, nonuniform structure as a means of obtaining a nonuniform activity profile.

NMR IMAGING THEORY

Applications of NMR spectroscopy are well-established in catalysis. This section provides an outline of the terms necessary to understand the imaging experiments described below and the data obtained from these experiments. More detailed descriptions of NMR imaging are given in Refs. (*6*) and (*7*). In NMR imaging, a magnetic field gradient, $\mathbf{G}$, is applied to the sample in addition to the uniform polarising field, $\mathbf{B}_0$. The resultant precessional frequency of the nuclear spins as a function of position, $\omega(\mathbf{r})$, is then given by

$$\omega(\mathbf{r}) = \gamma B_0 + \gamma \mathbf{G} \cdot \mathbf{r}, \qquad (1)$$

where γ is the gyromagnetic ratio and $\mathbf{r}$ is the position vector of the spins within the sample. It may be shown that the signal, dS, in an element of volume, dV, at position $\mathbf{r}$ with spin density $\rho(\mathbf{r})$ is given by (*7*)

$$dS(\mathbf{G}, t) = \rho(\mathbf{r})\, dV \exp[i(\gamma B_0 + \gamma \mathbf{G} \cdot \mathbf{r})t]. \qquad (2)$$

Thus the density of spins is observed as a function of real-space position $\mathbf{r}$ and, in principle, all the techniques of solid- and liquid-state NMR may be modified to give spatially resolved information. The imaging pulse sequences used in this study are based on the spin warp technique (*32*). Resolution of the order of 10–20 μm is obtained in the x–y plane, and this information is averaged, in the z-direction, over the slice "thickness" selected; in the images obtained in this work image slice thicknesses are typically about 0.3 mm. Figures 1a and 1b show the two modifications of the basic spin warp sequence used here: (a) the spin-echo and (b) the gradient-reversal imaging pulse sequences. The slice-selective pulse indicated at the beginning of each sequence takes the form of an rf pulse applied in the presence of a gradient, $\mathbf{G} = G_z$, which acts to selectively excite spins in a particular plane, the thickness of which can be controlled. The spatial resolution in the x- and y-directions is obtained using two perpendicular, linear gradients such that $\mathbf{G} = (G_x, G_y)$. These gradients are represented in Fig. 1 and are called the "read" and "phase-encoding" gradients. The resolved map of spin density, $\rho(\mathbf{r})$, may be obtained from the time domain signal, $S(\mathbf{k})$, by the Fourier transform

$$\rho(\mathbf{r}) = \iiint S(\mathbf{k}) \exp[-i2\pi \mathbf{k} \cdot \mathbf{r}]\, d\mathbf{k} \qquad (3a)$$

$$S(\mathbf{k}) = \iiint \rho(\mathbf{r}) \exp[i2\pi \mathbf{k} \cdot \mathbf{r}]\, d\mathbf{r}, \qquad (3b)$$

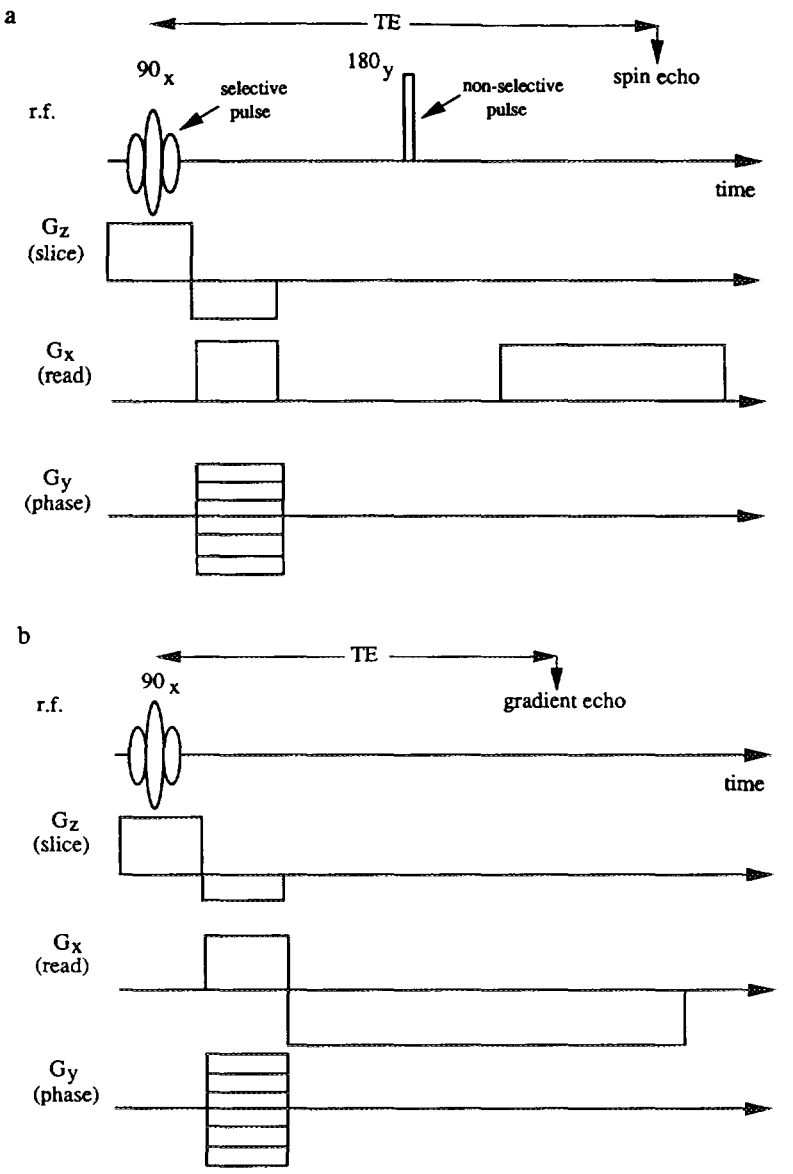

FIG. 1. NMR imaging pulse sequences for (a) spin-echo and (b) gradient-reversal methods.

where $\mathbf{k}$ is the reciprocal space vector defined by

$$\mathbf{k} = (2\pi)^{-1}\gamma \mathbf{G} t. \qquad (4)$$

An important concept to be appreciated in NMR imaging studies is that of spin relaxation and a very brief introduction to relaxation phenomena is given here. The application of an rf pulse to the spin system disturbs the equilibrium spin population distribution, and results in nutation of the magnetisation vector away from its equilibrium alignment with $\mathbf{B}_0$, conventionally taken to be along the z-direction, thereby giving rise to components of both transverse and longitudinal magnetisation relative to the equilib-

rium vector, $\mathbf{M}_0$. The exponential recovery of the longitudinal component of the magnetisation to its equilibrium value is known as spin–lattice relaxation and occurs via the transfer of excess energy from the spin population to its surroundings (commonly referred to as the "lattice"). The time constant of the relaxation process is therefore known as the spin–lattice (or longitudinal) relaxation time, T_1. The approach to thermal equilibrium in the *xy*-plane is described by a time constant, T_2, known as the spin–spin or transverse relaxation time; this mechanism arises predominantly from interactions between spins. In the context of this study we exploit the observation that the relaxation characteristics of a liquid confined in a porous solid will reflect the physical and chemical environment of that liquid phase; in particular, the rates of both relaxation mechanisms are enhanced in a liquid contained within a porous solid due to interactions at the solid–liquid interface (*33*) and therefore are sensitive to the pore structure of the material. The characteristic relaxation times of the sample influence the intensity of the NMR signal acquired and, as a result, it is possible to obtain images of the relaxation parameters themselves. Variations of relaxation time within the sample may then be correlated with variation in the physical and chemical environments within the sample; this point is discussed in more detail later in the paper. The effect of relaxation phenomena on signal intensity, the acquired signal in these experiments being referred to as an "echo," may be outlined as follows in the context of the spin-echo experiment (Fig. 1a). First, the echo amplitude will be modified by signal loss due to T_2 relaxation. In particular, if the echo is formed at a time TE after the creation of transverse magnetisation by the first 90° pulse, the echo amplitude is attenuated by the factor $\exp(-\mathrm{TE}/T_2)$. In addition the influence of T_1 will depend on the repetition time, TR, in the pulse sequence which is the time between each of the phase-encode steps in the sequence. If TR is not of the order of $5T_1$ or greater, complete recovery of the equilibrium magnetisation will not have occurred and a further attenuation of the image intensity due to spin–lattice relaxation, given by the factor $(1 - \exp(\mathrm{TR}/T_1))$, will be introduced. The gradient-reversal sequence differs from the spin-echo sequence in that only phase shifts due to the gradient are reversed in the former, and therefore contribute to the echo, whereas in the spin-echo sequence all shifts arising from Zeeman-like interactions are refocussed. Thus inhomogeneous effects such as field inhomogeneity, chemical shift, and susceptibility effects are not refocussed in the gradient-echo experiment and the image will be attenuated according to the observable decay of the NMR signal, $\exp(-\mathrm{TE}/T_2^*)$, where T_2^* describes the decay of the time domain NMR signal. The existence of magnetic susceptibility variations within a sample may therefore be studied by comparing images of the same sample obtained by both spin-echo and gradient-reversal pulse sequences; susceptibility variations within a sample (associated with defects or other heterogeneities) are highlighted in the gradient-reversal image.

From the above discussion it is clear that in many cases the image does not contain a quantitative representation of the spin density, $\rho(r)$, through the given image slice. Instead a modified spin density $C(r)\rho(r)$ is imaged, where $C(r)$ is a contrast mechanism (*7*) containing contributions ("weightings") from T_1 and T_2. From these data it is possible to extract information on the T_1 and T_2 characteristics themselves. Contrast effects should not necessarily be considered an inconvenience and it is often of interest to design experiments such that quantitative images of both the spin density and a particular contrast parameter are obtained. This may be achieved in two ways. The first approach develops from the relationship between image pixel intensity, S, and relaxation parameters given by Callaghan (*7*) for the spin-echo and gradient-reversal sequence as noted below.

gradient-reversal

$$S(\mathbf{r}) = \rho(\mathbf{r})\frac{\{1 - \exp(-\mathrm{TR}/T_1)\}\exp(-\mathrm{TE}/T_2^*)}{1 - \cos\theta\exp(-\mathrm{TR}/\mathrm{T}_1)}\sin\theta; \quad (5)$$

spin-echo

$$S(\mathbf{r}) = \rho(\mathbf{r})\frac{[1 - 2\exp\{(-(\mathrm{TR} - \mathrm{TE}/2)/T_1)\} + \exp(-\mathrm{TR}/T_1)]\exp(-\mathrm{TE}/T_2)}{1 + \cos\theta\exp(-\mathrm{TR}/T_1)}\sin\theta. \quad (6)$$

Here θ is the pulse angle of the first radio-frequency pulse. In Fig. 1, the first pulse is specified as 90°. By acquiring a sequence of images where TE or TR is varied, the appropriate function for the pulse sequence may be fitted to the set of images and maps of T_1, T_2, and T_2^* obtained. Alternatively, the spin system may be preconditioned with a pulse sequence that develops contrast due to a particular mechanism. For example, if a quantitative image of T_1 is required, a saturation recovery pulse sequence (*34*) (a pulse sequence used to measure T_1 in a 1D spectroscopy experiment) is added to the front end of the appropriate imaging sequence. Similarly, if a map of the self-diffusion coefficient is required the PGSE sequence (*35*) is used to precondition the imaging sequence. The preconditioning approach is used in this work.

EXPERIMENTAL

Sample Characterisation and Preparation

A range of porous alumina and silica catalyst support pellets of spherical and cylindrical geometry were studied as listed in Table 1. Nominal pellet dimensions are also given in the table. Nitrogen adsorption and mercury porosimetry analyses were performed using a Micromeritics ASAP 2000 and a Micromeritics Autopore II 9220, respectively. A summary of the characterisation results is given in Table 1 and the cumulative mercury intrusion curves are given in Fig. 2. All samples had pore sizes lying in the range 1–1000 nm.

Samples for NMR imaging were prepared by impregnating catalyst pellets with deionised water for at least 12 h under ambient conditions. Excess water was removed from the pellet external surface by contacting each pellet with presoaked filter paper (Whatman No. 1). The paper was wetted in order to prevent any liquid being removed from within the pores of the pellet. The pore water content was determined gravimetrically and, as shown in Table 1, the void volume so obtained was consistent with complete void filling based on the porosimetry data within an experimental uncertainty of ±5%. Selected samples were also impregnated under vacuum conditions and the results so obtained were in close agreement with those obtained from samples prepared under ambient conditions. Single pellets were placed in a glass NMR sample tube and a glass rod used to fill the air space above the pellet to prevent sample drying. The sample tube was sealed and successive weighings over a period of several days showed that water loss due to drying was less than 1%.

The experimental data presented here include both spatially resolved and nonresolved measurements, the conventional terms used to discriminate between imaging and spectroscopy experiments. In the first instance, nonresolved data were acquired to characterise the relaxation parameters T_1, T_2, and T_2^* such that the imaging experiments could be designed accordingly. Nonresolved measurements of T_1 and diffusion coefficient were also obtained for comparison with the data obtained from the spatially resolved (imaging) experiments. All NMR experiments were performed using a Bruker Spectrospin MSL 200 NMR spectrometer.

TABLE 1

Characterisation of Porous Catalyst Support Pellets

Sample	Material	Nominal diameter (mm)	Pellet form	Characterisation technique				Water impregnation[a]
				BET	Mercury porosimetry			
				Surface area ($m^2\ g^{-1}$)	Surface area ($m^2\ g^{-1}$)	Pore volume ($ml\ g^{-1}$)	Porosity (%)	Pore volume ($ml\ g^{-1}$)
E2	Alumina	3.0	Extrudate	182	250	0.67	65	0.69
E3	Alumina	3.0	Tablet	120	134	0.44	59	0.42
I1	Alumina	10.0	Tablet	2.4[b]	2.3	0.19	39	0.19
P1	Silica	1.0	Extrudate	194	267	1.14	70	—
S1	Silica	3.0	Gel sphere	160	224	0.94	60	0.96
S2	Silica	2.2	Gel sphere	65	97	0.77	61	0.76

[a] Water impregnation under ambient conditions.
[b] Surface area too small for accurate measurement by nitrogen adsorption.

The magnet had a static field strength of 4.7 T, yielding a proton resonant frequency of 200.13 MHz. Data acquisition was controlled by an Aspect 3000 computer.

NMR relaxation measurements were performed using a Bruker Spectrospin Z32-VSP 200 ^{1}H 7.5 probe tuned to 200.13 MHz. The 90° rf pulse duration was approximately 15 μs. The relaxation properties of each sample were determined and are given in Table 2. These results are in close agreement with those obtained on a probe with a 5-mm coil and a typical 90° rf pulse duration of 4 μs. The reported values give the best fit to the experimental data and are averages over three or four samples consisting of between 1 and 50 catalyst pellets depending on the pellet size. The relaxation times were determined according to standard methods (*34*): spin–lattice (T_1) relax-

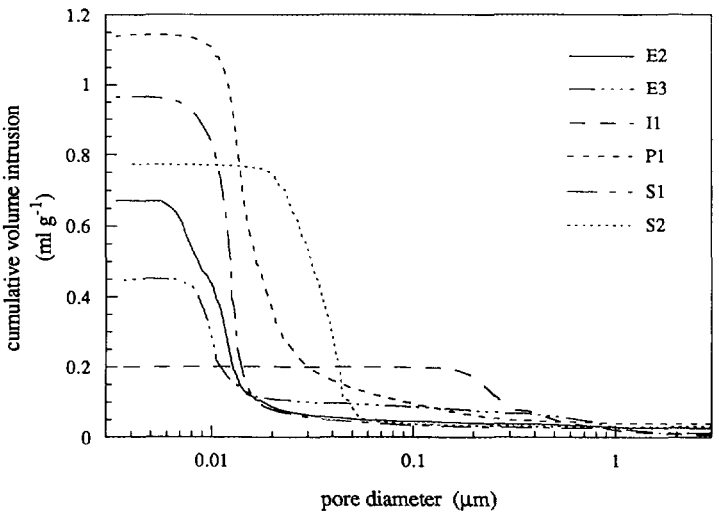

FIG. 2. Cumulative mercury intrusion curves obtained from porosimetry characterisation of the samples given in Table 1.

TABLE 2

NMR Relaxation Characteristics of Porous Catalyst Support Pellets Obtained from Spatially Nonresolved Measurements

Sample	T_2^* (ms)	T_2 (ms)	T_1 (ms)
E2	1.1	4.4	280
E3	1.2	4.0	260
I1	1.0	5.2	240
P1	5.0	—	660
S1	1.6	11.0	145
S2	3.8	43.0	426

ation times were determined using the inversion-recovery method, spin–spin (T_2) relaxation times by the Hahn echo method, and the T_2^* was determined from the spectral linewidth at half maximum. The contribution to the line-width due to magnetic field inhomogeneity was less than 10 Hz. Multi-exponential relaxation behaviour was observed for the samples, corresponding to stretched-exponential indices typically in the range 0.85 to 0.99. In the case of transverse relaxation, the cited values of T_2 are given in order to indicate the degree of echo attenuation as a function of image echo time for the spin-echo sequence: a more rigorous analysis of the intrinsic T_2 would need to account for the effect of diffusion in the presence of susceptibility-induced gradients using the CPGM pulse sequence over a range of pulse spacings.

Clearly, very fast relaxing components of the magnetisation will not contribute to the echo, and will not be detected by NMR imaging. These may be due to spins in water bound to the pore surface and not averaged over the pore volume by diffusion during the echo time. Comparison of the initial intensity of the free induction decay (FID) following a 90° pulse with the echo intensity for both pure water and the saturated pellets showed that 90 to 98% of the water was detected at the echo times employed in the imaging experiments.

NMR Imaging

^{1}H NMR imaging experiments were conducted using a Bruker microimaging unit. Shielded gradient coils were used and an air flow was maintained through these in order to prevent overheating arising from rapid gradient switching. A range of imaging probe insert sizes was available with diameters from 2 mm (solenoid coil) to 5–25 mm (saddle and resonator coils). The maximum attainable gradient strength was 51 G cm^{-1} (1 G = 10^{-4} T). For each imaging probe insert, the response of the imaging coil as a function of position was determined for a sample of water and was uniform over the volume occupied by catalyst pellet samples. Fourier transformation of the data to obtain the image was performed on the Aspect 3000 computer, which included an array processor, and images were transferred to a Sun IPX SPARC station for further processing including function fitting and multi-image display.

Slice selection was obtained using Gaussian rf pulses truncated at 10% of maximum intensity. The slice gradient was typically 8 G cm^{-1} and the gradients in the read and phase encoding dimensions were in the range 10 to 40 G cm^{-1}. The slice thickness never exceeded 20% of the pellet diameter. In each case the pellet was positioned so that the image slice passed through the centre of the pellet; this was particularly important for spherical pellets. The stability in water content of the sample during the course of the imaging experiment was monitored by comparing the signal from a simple "pulse-acquire" sequence before and after the image acquisition. In all cases the intensity of the final observation was within ±5% of the first. The image acquisition time for single images was a maximum of thirty minutes, although for experiments requiring multi-image acquisition (T_1 and D maps), the total acquisition time was as long as 16 h.

In addition to the small sample volumes (0.01–0.7 cm^3 compared to 2–1000 cm^3 in (*16, 21*)), the rapid transverse relaxation time of the samples required rapid gradient switching times in order to minimise the echo time and loss of signal due to transverse relaxation. As a result, gradient pre-

emphasis was required for the z-gradient (slice direction) in order to minimise interference between the spin-echo and induced eddy currents. All imaging procedures, and in particular the relaxation and diffusion methods, were validated using liquid phantoms.

Relaxation and Diffusion Imaging

Images of the T_1 relaxation time and diffusivity of the imbibed water were obtained by preconditioning the spins with saturation-recovery and stimulated echo PGSE pulse sequences, respectively. In each case, 8 to 12 images were acquired at different values of the appropriate variable in each experiment. To obtain a T_1 image the signal intensity S from the same pixel, i, in each image is fitted to the expression describing the magnetisation recovery appropriate to the saturation recovery experiment (*34*),

$$S(i, \tau) = \rho(i)[1 - \exp\{-\tau/T_1(i)\}], \quad (7)$$

where τ is the delay time in the saturation-recovery preconditioning pulse sequence, thereby obtaining a value of T_1 and ρ for that pixel, i.e., $T_1(i)$ and $\rho(i)$. By repeating this procedure for each pixel in the image a complete map of relaxation time and spin density within the sample is produced. It is noted that the spin density map will still contain some contrast associated with the imaging sequence following the preconditioning sequence. A map of liquid diffusivities within the pellet is obtained using a similar approach, this time fitting the following expression appropriate to the PGSE preconditioning sequence:

$$M(i, \delta) \propto \exp[-D(i)\gamma^2 g^2 \delta^2(\Delta - \delta/3)]. \quad (8)$$

Here $D(i)$ is the value of diffusivity assigned to pixel i, g is the pulsed gradient strength in G cm^{-1}, δ is the duration of the pulsed gradient, and Δ is the diffusion time (*35*). The pulsed gradient of 47.6 G cm^{-1} was produced by the z-axis (slice) gradient coils and images were acquired at values of δ ranging between 0.2 and 1.5 ms.

T_1 and diffusion preconditioned images contain noise which leads to uncertainty in the fitted T_1 and diffusion images. In the fitting procedure, pixel intensities less than a threshold given by three times the image rms noise level were omitted from the fitting procedure, and pixels were rejected from the fitting procedure if more than the three least significant points were omitted from a given fit. This was most likely for regions of the image with low intensity and in particular for pixels at the periphery of the pellet. The relative errors (90% confidence) in the fitted values of T_1 and D were less than 10% for accepted pixel fits.

RESULTS AND DISCUSSION

Single NMR Images

Gradient-reversal slice images for single catalyst pellets are shown in Fig. 3. In each image, maximum pixel intensity (white) corresponds to maximum signal and moisture content (voidage). The images are subject to varying degrees of T_1 and T_2 relaxation contrast according to the values of TE and TR given in the caption, the relaxation properties given in Table 2 and the contrast function given by Eq. (5). Whether due to variations in voidage or locally varying relaxation times, all images show heterogeneity to some degree. The effect of varying TE is apparent from Figs. 3a and b where two pellets from the same sample batch have been imaged with varying TE and constant TR. Some of the differences between these two images may result from variability within a batch and this point is discussed later. Internal heterogeneity in the structure is most clearly apparent in Fig. 3b where the longer echo time has increased the degree of T_2-weighting. Figure 3c is an image taken through a 3-mm-diameter alumina extrudate. Two regions of high and low intensity reflecting high and low water content within the sample are clearly seen. The high-intensity region at the external surface of the pellet is probably a result of the extrusion process used in the formation of the pellet; this feature is absent from pellets formed by tabletting (Fig. 3e). At 1.0 mm in diameter, sample P1 is the smallest sample imaged in this study and is shown in Fig. 3d. A clear

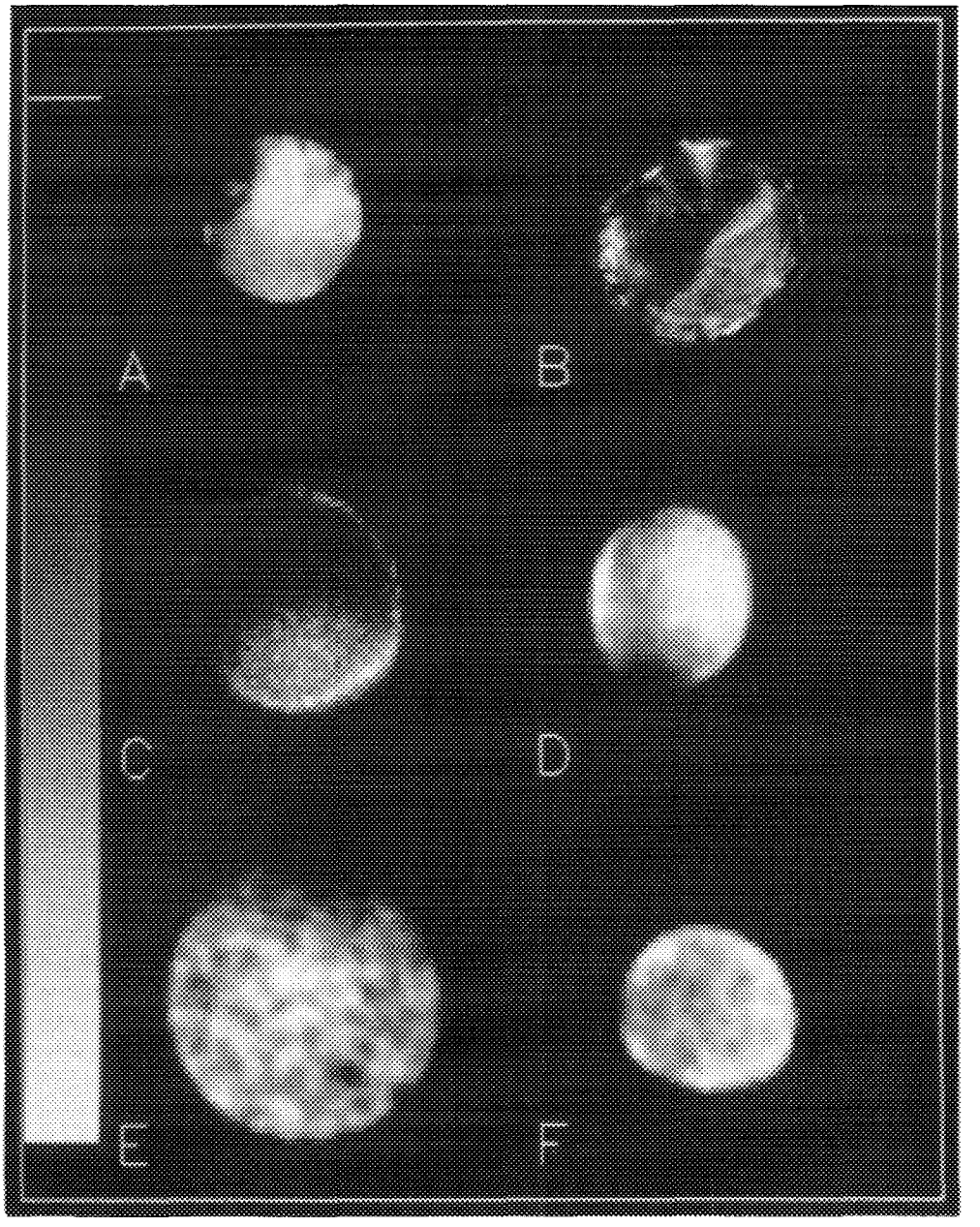

FIG. 3. Gradient-reversal images for single water-saturated pellets from the samples given in Table 1: (a) sample S1 (128 × 128, 0.6 mm slice, pixel = (41 μm)^2, TE = 2.0 ms, TR = 100 ms), (b) sample S1 (128 × 128, 0.6 mm slice, pixel = (41 μm)^2, TE = 11.6 ms, TR = 100 ms), (c) sample E2 (64 × 64, 0.6 mm slice, pixel = (70 μm)^2, TE = 1.5 ms, TR = 50 ms), (d) sample P1 (64 × 64, 0.2 mm slice, pixel = (31 μm)^2, TE = 4.0 ms, TR = 50 ms), (e) sample E3 (64 × 64, 0.3 mm slice, pixel = (58 μm)^2, TE = 1.5 ms, TR = 300 ms), and (f) sample S2 (64 × 64, 0.3 mm slice, pixel = (67 μm)^2, TE = 1.5 ms, TR = 300 ms).

band of low intensity exists through the middle of this pellet, again perhaps due to uneven compression of the material in the extrusion process. Figures 3e and f are from samples E3 and S2 with reduced T_2- and T_1-weighting. These also show the existence of

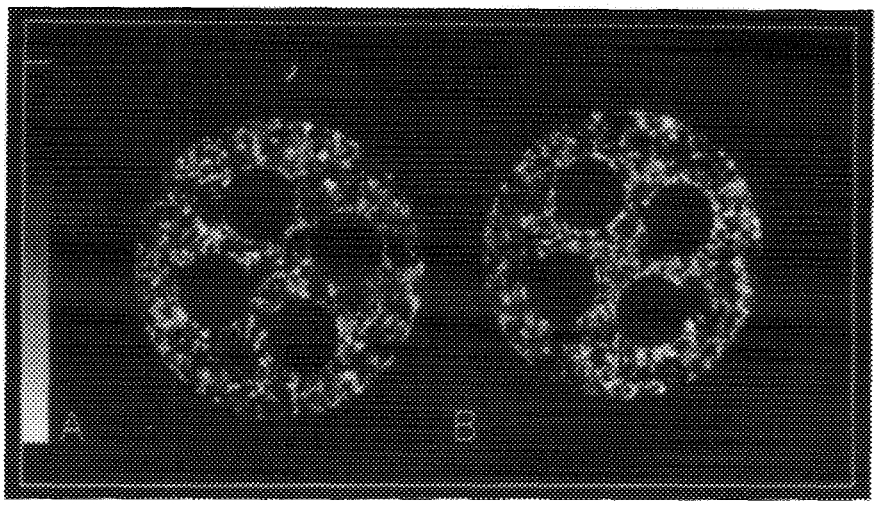

FIG. 4. Images of a pellet from batch I1—slice location and sample orientation vary: (a) gradient-reversal image and (b) spin-echo image (128 × 128, 1.0 mm slice, pixel = (103 μm)^2, TE = 1.9 ms, TR = 200 ms).

internal heterogeneity. These experiments demonstrate that if only single NMR images are acquired, it will always be ambiguous as to which mechanism is causing the observed contrast (variations in voidage and/or relaxation properties). However, whatever the cause, it is clear that the samples do contain heterogeneities on a size scale much greater than the mean pore-size.

Before proceeding, it is important to confirm that the heterogeneity observed in Fig. 3 does indeed result from relaxation as opposed to susceptibility variations (perhaps caused by paramagnetic species) within the sample. Therefore both gradient-reversal and spin-echo images of the same samples were acquired; an example of the results obtained is shown in Fig. 4 for a 10-mm-diameter pellet containing four 3 mm diameter holes, which are clearly visible in the images. The images shown were obtained from the same pellet, although slice location and sample orientation vary between the two experiments. Clearly the two images are very similar suggesting that the heterogeneities observed are not associated with magnetic susceptibility variations within the catalyst pellet. Similar observations were made for the support materials in Fig. 3. In a previous study (*14*) where significant differences were observed between spin-echo and gradient-reversal images, the pore size in the sample was of the same order of size as the image pixel dimension. In that work, it was argued that the magnetic susceptibility boundary arising at the solid/liquid interface would lead to a magnified susceptibility artifact in the gradient-reversal image. In all the samples given in Table 1, the pore size is orders of magnitude smaller than the pixel dimension and so each pixel contains many pores. Therefore, the effect of susceptibility boundaries will be averaged over the pixel volume, resulting in an overall reduction in T_2^* and no susceptibility contrast between neighbouring pixels. Thus, any contrast in the NMR images shown in Figs. 3 and 4 is most likely due to variations in the local pore structure (void fraction, pore-size) across the pellet.

Spatial Resolution of T_1 and D

The results obtained by fitting Eqs. (7) and (8) to multiple image data sets obtained from T_1 and PGSE preconditioned gradient-reversal imaging datasets are shown in Figs.

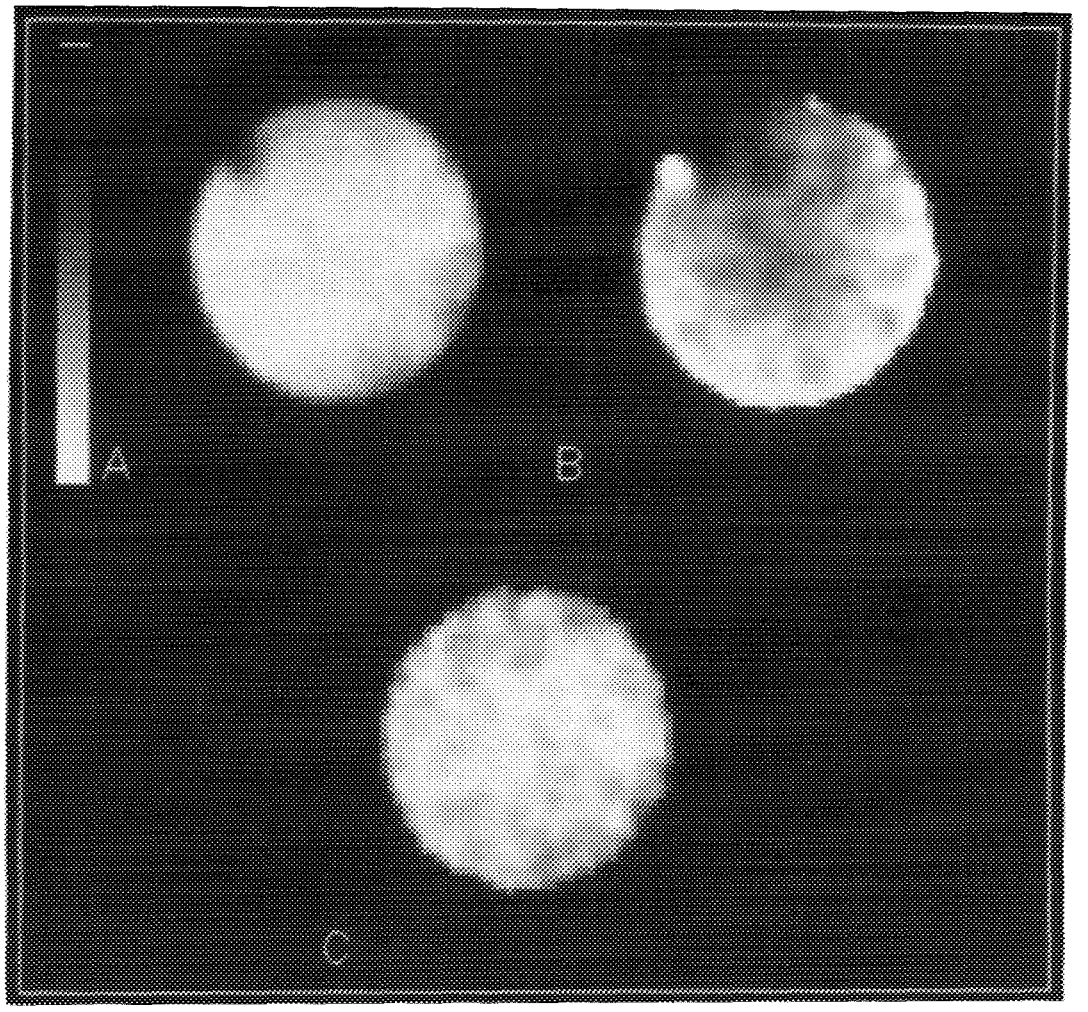

FIG. 5. Density, T_1 and diffusivity images for a 2.2-mm nominal diameter silica sphere from batch S2 obtained by fitting Eqs. (7) and (8) to eight T_1 preconditioned and eight PGSE preconditioned images: (a) fitted ρ map from T_1 preconditioning, (b) fitted T_1 map (scale = 150–400 ms), and (c) fitted diffusivity map (scale = 0–1.5 × 10^{-9} m^2 s^{-1}) (64 × 64, 0.3 mm slice, pixel = (45 μm)^2, TE = 1.5 ms, TR = 750 ms).

5–7. As before, the maximum pixel intensity corresponds to either maximum spin density, large T_1 (i.e., slow relaxation due to a large local mean pore-size), or fast diffusion in the relevant images. For relaxation (b) and diffusivity (c) images, the range of values represented by the linear grey-scale is given in the captions. Although the lower limit on the scale in Figs. 5c to 7c is zero, we emphasize that in the current experimental configuration, the lowest accessible diffusivity is about 1.0 × 10^{-10} m^2 s^{-1}. Results are shown only for samples S1 and S2 because T_2 in these samples is long enough to allow a sufficient range of the pulsed gradient time, δ, in Eq. (8) to be applied in order to obtain the diffusion coefficient, D, with adequate precision. In each case, the den-

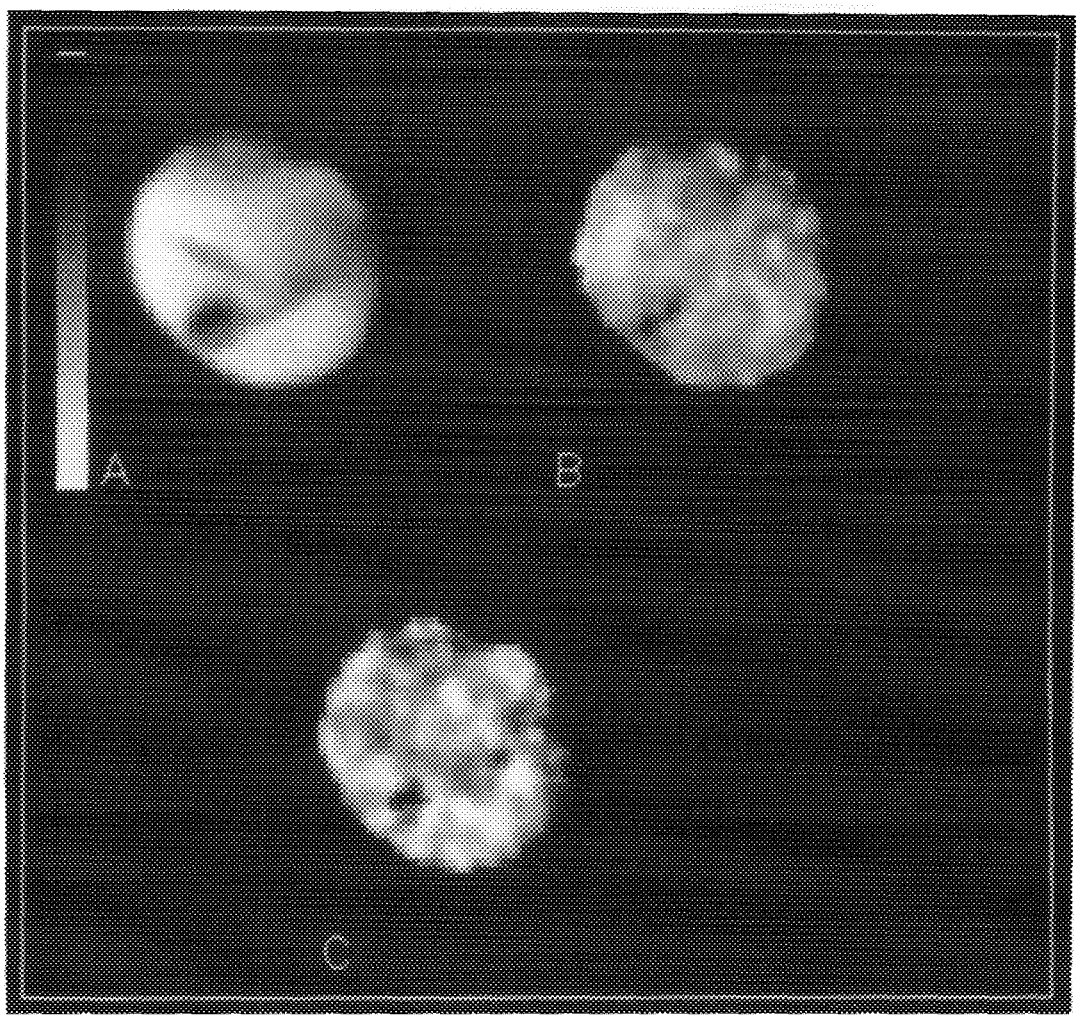

FIG. 6. Density, T_1 and diffusivity images for a 2.2-mm nominal diameter silica sphere from batch S2 obtained by fitting Eqs. (7) and (8) to eight T_1 preconditioned and eight PGSE preconditioned images: (a) fitted ρ map from T_1 preconditioning, (b) fitted T_1 map (scale = 150–400 ms), and (c) fitted diffusivity map (scale = 0–1.5 × 10^{-9} m^2 s^{-1}) (64 × 64, 0.3 mm slice, pixel = (45 μm)^2, TE = 1.5 ms, TR = 750 ms).

sity map shown is the image of preexponential factors obtained from the T_1-preconditioned experiment as defined in Eq. (7). It is noted that even when TE is short and TR long in these experiments, the density images will still contain some contrast due to T_1 and T_2^* in the resolution part of the imaging sequence, as given by Eq. (5). The mean values of the relaxation time and diffusivity in each image are given in Table 3, where they are compared with the results obtained from spatially nonresolved inversion-recovery and stimulated echo PGSE experiments.

The images in Figs. 5 and 6 were obtained with constant acquisition parameters for two pellets from batch S2: these are referred to as samples S2.1 and S2.2, respectively. The apparent structures of these two pellets, indicated by spin density, T_1, and diffusivity

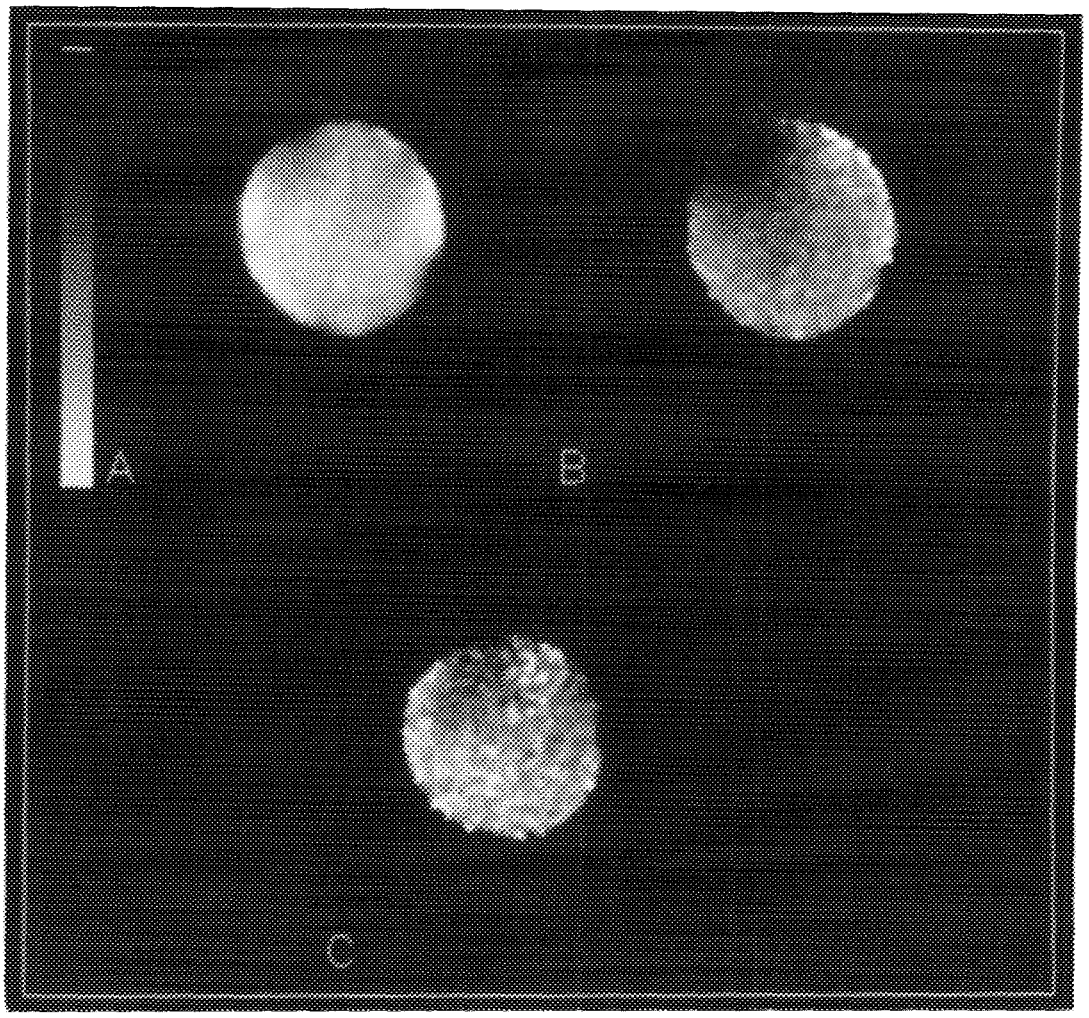

FIG. 7. Density, T_1 and diffusivity images for a 3.0-mm nominal diameter silica sphere from batch S1 obtained by fitting Eqs. (7) and (8) to eight T_1 preconditioned and eight PGSE preconditioned images: (a) fitted ρ map from T_1 preconditioning, (b) fitted T_1 map (scale = 70–350 ms), and (c) fitted diffusivity map (scale = 0–1.2 × 10^{-9} m^2 s^{-1}) (128 × 128, 0.3 mm slice, pixel = (41 μm)^2, TE = 1.8 ms, TR = 600 ms).

images, are significantly different. Histograms of the distribution of diffusivities in the pellets are given in Fig. 8. The range of diffusion coefficients observed is consistent with the self-diffusion of water in the pellet being restricted compared with that of bulk water which has a diffusivity of 2.0 × 10^{-9} m^2 s^{-1} at 294 K. Pellet S2.1 has a relatively uniform liquid distribution compared with pellet S2.2, where regions of high and low voidage are apparent. Despite the relatively uniform voidage, pellet S2.1 still contains significant heterogeneity in the T_1 and diffusivity maps (Figs. 5b and c). Further, while the scale of the heterogeneities is consistent between the T_1 and diffusivity maps of this pellet, there does not appear to be a simple relationship between the values of these two parameters. Pellet S2.2 (Fig. 6) has a more heterogeneous voidage and the structure ap-

TABLE 3

Comparison of T_1 Relaxation Times and Diffusivities Obtained from NMR Images and from Nonresolved (nr) Measurements

Pellet	Figure	$\overline{T}_{1\,\text{image}}$ (ms)	$T_{1\,\text{nr}}$[a] (ms)	$\overline{D}_{\text{image}}$ (10^{-9} m^2 s^{-1})	D_{nr}[b] (10^{-9} m^2 s^{-1})	$(\sigma/\mu)_{D\,\text{image}}$[c]
S2.1	5	317	376	1.2	1.47 ± 0.04	0.10
S2.2	6	270	313	1.1	1.47 ± 0.04	0.20
S1	7	218	140	0.92	1.27 ± 0.06	0.19

[a] From a nonresolved relaxation experiment on the single pellet.
[b] Average diffusion coefficient over three samples of >20 pellets.
[c] Reduced standard deviation from histograms in Fig. 8; σ and μ are the standard deviation and mean, respectively.

parent in the T_1 and diffusivity maps follows this more closely.

The diffusional heterogeneity of the pellets may be quantified by calculating the reduced standard deviation, $(\sigma/\mu)_D$, of the distribution of pixel diffusivities shown in the histograms in Fig. 8: $(\sigma/\mu)_D$ is 0.10, 0.20, and 0.19 for pellets S2.1, S2.2, and S1, respectively. For a homogeneous medium, the expected reduced standard deviation based on the error in the fits (10% at 90% confidence) has an upper bound of 0.06. The widths of all the experimental distributions are significantly greater than this suggesting that there are significant heterogeneities within the samples at the size scale observed. In fitting the diffusion-weighted images for pellet S2.2, three pixels in the low-intensity region at the lower left of the image (Fig. 6c) were omitted from the fitting procedure as specified above and were assigned a value of zero.

Pellet S1 (Fig. 7) shows a relatively homogeneous voidage and the structures apparent in the T_1 and diffusivity maps are again consistent in scale. These results show that significant spatial variations exist not only within a given pellet but also between different pellets from the same batch. This illustrates the potential of NMR imaging as a quality control technique in the processing of support materials, particularly where materials of uniform voidage and structure are required.

Comparison of average values of T_1 and diffusivity from the images with those obtained from the simple nonresolved experiments given in Table 3 shows that there are discrepancies between the two methodologies. This has also been observed by Attard *et al.* (*17*) in the imaging of brine-saturated oil reservoir cores. A possible reason for these observations is suggested as follows. In the case of the imaging experiments, the image arises from a central slice in the pellet, in this case comprising only about 10 to 20% of the pellet volume. By contrast, the entire pellet contributes to the signal in the nonresolved experiment: relaxation times ($T_{1\,\text{nr}}$) were obtained from the same pellets as shown in Figs. 5 to 7, and nonresolved diffusivities (D_{nr}) are the average of three samples each containing about twenty pellets. In addition, Figs. 5 and 6 and Table 3 show that there are significant variations between different pellets from the same sample batch. This sampling discrepancy could be eliminated by imaging more pellets without slice selective imaging. Density and T_1 images presented by Smith *et al.* (*27*) of sol–gel materials during gel formation, were obtained without slice selection. However, the ability to observe structural inhomogeneity is reduced in this case since the signal is averaged along the entire length of the pellet. We suggest that slice imaging is a more appropriate technique in deducing the existence of pellet heterogeneity. Structural in-

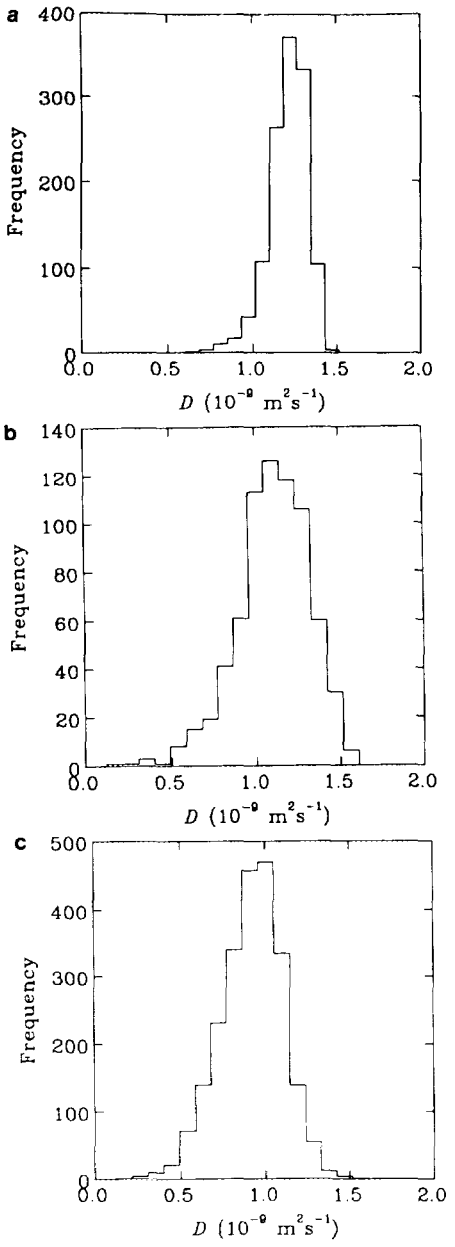

FIG. 8. Diffusivity histograms (a)–(c) for the PGSE images in Figs. 5c to 7c, respectively. The frequency axis represents the number of pixels with diffusivity, D.

formation throughout the entire pellet could be obtained via three-dimensional imaging; however, on samples such as catalyst supports the acquisition times become very long if T_1 and diffusivity images are to be obtained.

The Relationship between T_1 and Pore Structure

Earlier, it was noted that the relaxation times T_1 and T_2 will reflect the physicochemical environment of the liquid phase. However, direct correlation of the relaxation time constants and any particular physicochemical parameter is not straightforward, particularly in the case of T_2. In contrast, many workers have attempted to correlate the distribution of spin–lattice relaxation times within a sample to the pore-size distribution of that sample. It is noted that the majority of these studies have used spatially non-resolved relaxation time measurements (*36*, *37*). The relation between T_1 and the hydraulic pore radius (2 × pore volume/pore surface area), r, (in the fast-exchange limit appropriate to the conditions under which these experiments are performed (*38*)) is given by

$$\frac{1}{T_1} = \alpha + \frac{\beta}{r}, \qquad (9)$$

where α and β are constants characteristic of the sample under study. Thus variations within the T_1 image will correlate with heterogeneity in mean pore size within the sample. Assuming the validity of equation (9), the heterogeneity in the images shown in Figs. 5b–7b indicates that the local mean pore size varies significantly throughout the pellet. It is important to remember that within each image pixel a distribution of pore sizes exists, and that the T_1 of any given pixel reflects the mean pore size within that pixel. These observations raise interesting questions as to how the results of more conventional methods of pore-structural characterisation are interpreted in the theoretical representation of porous media.

In existing models, an experimentally obtained pore-size distribution is applied to the model by randomly assigning pore dimensions to a network of pores of some specified shape. In some cases, the model may relate

to a particular type of structure such as porous sinters (*39*) or bidisperse structures (*40*). In most cases reported to date it has been assumed that the pore-size distribution obtained from, for example, nitrogen adsorption or mercury porosimetry experiments is representative of a macroscopically homogeneous pore structure with local variation in pore size over length scales of the order of the pore dimension. The T_1 images of the porous pellets examined in this study suggest that macroscopic heterogeneities in pore structure make a significant contribution to the pore-size distribution obtained in spatially nonresolved measurements. As a result NMR images, such as those presented here, provide complementary information to that obtained by conventional characterisation techniques.

Smith *et al.* (*27*) have suggested that fitting a distribution of relaxation times (hence pore sizes) to each pixel in a set of relaxation-weighted images may be used to obtain the pore-size distribution at each pixel within the image. While this would be an interesting extension of the technique, there are two important limitations. Firstly, diffusion over the time TE would average the relaxation times over the pores contained within the volume defined by the rms diffusive displacement (typically 1–10 μm). For catalyst support materials such as those given in Table 1, this diffusion-averaged volume is about three orders of magnitude greater than the mean pore size; thus it is only possible to obtain a locally diffusion-averaged pore-size using this approach. Secondly, as pointed out in nonresolved studies (*36, 37*), the deconvolution of multiple relaxation times from an experimental data set is very sensitive to the signal-to-noise ratio. The required image acquisition time to achieve adequate signal-to-noise ratio in experiments of the nature described in this study would be prohibitive. Spectrometer and gradient stability over such long time scales may also be limiting.

Pore Structure and Transport

Insofar as the spin density and T_1 images reflect the pellet structure, the NMR images demonstrate that the transport properties (e.g., diffusion) within a pellet are influenced by the local pellet structure. In particular, it is noted that the length scales of the heterogeneities in T_1 and diffusivity images are consistent in each of Figs. 5–7. The relationship between the pore structure and the transport processes occurring within it is a fundamental question. It is not yet possible to take a characterisation of a porous solid, translate that characterisation to a theoretical representation of the medium and then use the same model to predict transport phenomena. Resolution of this problem is unlikely to be achieved while characterisation and transport measurements are made under widely disparate conditions. For example, pore-size analysis may be performed by impregnating a porous material with mercury (a dense, nonwetting liquid), while the diffusivity of a gas through a porous pellet is commonly measured using a Wicke–Kallenbach experiment. Such problems may, at least in part, be overcome by the use of a combination of NMR techniques to study a single sample under constant physical conditions: NMR can be used to measure *both* structural (i.e., relaxation and voidage) and transport (i.e., diffusion and flow) phenomena. Moreover, the NMR experiments described here are performed under steady-state conditions, removing the need to describe accurately the condensation, percolation and intrusion mechanisms encountered in conventional techniques (*41*).

CONCLUSIONS

The use of a range of NMR imaging techniques on liquid soaked catalyst support pellets allows the large scale structure of these pellets to be examined. Significant variations exist in the local voidage, pore size, and, as a consequence, liquid diffusivity. In addition to variations between different types of support materials, the observed

structures vary significantly between pellets from the same sample batch. It is suggested that NMR imaging experiments provide a convenient tool for characterising porous catalyst supports and also may have more general application in the quality control of catalyst support manufacture. The interrelationship between voidage and transport heterogeneity effects has been imaged directly.

The images presented in this paper reveal variations in local pore structure over size scales much larger than the pore size. Therefore we suggest that a combination of standard characterisation experiments, such as nitrogen adsorption and mercury porosimetry, in conjunction with NMR imaging, will lead to a more accurate representation of the porous structure. In particular, we suggest that as well as including a distribution of pore sizes on the microscopic scale, future developments in modelling porous materials should consider the existence of macroscopic structures and nonuniformity of voidage and their influence on catalyst performance.

ACKNOWLEDGMENTS

The authors gratefully acknowledge the Process Engineering Committee of the SERC for the award of an NMR spectrometer. M.P.H. thanks the Association of Commonwealth Universities for a Commonwealth Scholarship, and Trinity College, Cambridge, for a Rouse Ball Studentship. L.F. Gladden thanks ICI for the award of an ICI Fellowship and for their continuing interest in this work. We also thank Dr. P. Alexander for providing the image analysis software used in this study.

REFERENCES

1. Sahimi, M., Gavalas, G. R., and Tsotsis, T. T., *Chem. Eng. Sci.* **45,** 1443 (1990).
2. Hollewand, M. P., and Gladden, L. F., *Chem. Eng. Sci.* **47,** 1761 (1992).
3. Hollewand, M. P., and Gladden, L. F., *J. Phys.: Condens. Matter* **4,** 5757 (1992).
4. Becker, E. R., and Wei, J., *J. Catal.* **46,** 372 (1977).
5. Summers, J. C., and Hegedus, L. L., *J. Catal.* **51,** 185 (1978).
6. Mansfield, P., and Morris, P. G., "NMR Imaging in Biomedicine." Academic Press, New York, 1982.
7. Callaghan, P. T., "Principles of Nuclear Magnetic Resonance Microscopy." Oxford Univ. Press, Oxford, 1991.
8. Gummerson, R. J., Hall, C., Hoff, W. D., Hawkes, R., Holland, G. N., and Moore, W. S., *Nature* **281,** 56 (1979).
9. Rothwell, W. P., and Vinegar, H. J., *Appl. Opt.* **24,** 3969 (1985).
10. Hall, L. D., and Rajanayagam, V., *J. Magn. Reson.* **74,** 139 (1987).
11. Maudsley, A. A., Hilal, S. K., Perman, W. H., and Simon, H. E., *J. Magn. Reson.* **51,** 147 (1983).
12. Hall, L. D., Rajanayagam, V., and Hall, C., *J. Magn. Reson.* **68,** 185 (1986).
13. Majors, P. D., Smith, J. L., Kovarik, F. S., and Fukushima, E., *J. Magn. Reson.* **89,** 470 (1990).
14. Sarkar, S. N., Wooten, E. W., and Komoroski, R. A., *Appl. Spectrosc.* **45,** 619 (1991).
15. Chang, C., and Komoroski, R. A., *Macromolecules* **22,** 600 (1989).
16. Osment, P. A., Packer, K. J., Taylor, M. J., Attard, J. J., Carpenter, T. A., Hall, L. D., Herrod, N. J., and Doran, S. J., *Philos. Trans. Soc. London A Ser.* **333,** 441 (1990).
17. Attard, J. J., Carpenter, T. A., Hall, L. D., Davies, S., Taylor, M. J., and Packer, K. J., *Magn. Reson. Imaging* **9,** 815 (1991).
18. Rothwell, W. P., Holecek, D. R., and Kershaw, J. A., *J. Polym. Sci.* **22,** 241 (1984).
19. Blackband, S., and Mansfield, P., *J. Phys. C* **19,** L49 (1986).
20. Weisenberger, L. A., and Koenig, J. L., *J. Polym. Sci. Polym. Lett.* **27,** 55 (1989).
21. Majors, P. D., Smith, D. M., and Davis, P. J., *Chem. Eng. Sci.* **46,** 3037 (1991).
22. Kärger, J., and Ruthven, D. M., "Diffusion in Zeolites and Other Microporous Solids." Wiley, New York, 1992.
23. Redpath, T. W., Norris, D. G., Jones, R. A., and Hutchinson, J. M. S., *Phys. Med. Biol.* **29,** 891 (1984).
24. Callaghan, P. T., and Xia, Y., *Makromol. Chem. Macrol. Symp.* **34,** 277 (1990).
25. Callaghan, P. T., and Xia, Y., J. Magn. Reson. **91,** 326 (1991).
26. Jenner, C. F., Xia, Y., Eccles, C. D., and Callaghan, P. T., *Nature* **336,** 399 (1988).
27. Smith, D. M., Deshpande, R., Brinker, C. J., Earl, W. L., Ewing, B., and Davis, P. J., *Catal. Today* **14,** 293 (1992).
28. Hollewand, M. P., and Gladden, L. F., *Trans. IChemE* **70A,** 183 (1992).
29. Hollewand, M. P., Ph.D. dissertation, University of Cambridge, 1992.
30. Hollewand, M. P., and Gladden, L. F., submitted for publication.
31. Hollewand, M. P., and Gladden, L. F., *Magn. Reson. Imaging*, in press (1993).

32. Edelstein, W. A., Hutchison, J. M. S., Johnson, G., and Redpath, T., *Phys. Med. Biol.* **25,** 751 (1980).
33. Woessner, D. E., *J. Chem. Phys.* **36,** 1 (1962).
34. Fukushima, E., and Roeder, S. B. W., "Experimental Pulse NMR: A Nuts and Bolts Approach." Addison–Wesley, Reading, MA, 1981.
35. Stejskal, E. O., and Tanner, J. E., *J. Chem. Phys.* **42,** 288 (1965).
36. Gallegos, D. P., Munn, K., Smith, D. M., and Stermer, D. L., *J. Colloid Interface Sci.* **124,** 186 (1988).
37. Davies, S., Kalam, M. Z., Packer, K. J., and Zelaya, F. O., *J. Appl. Phys.* **67,** 3171 (1990).
38. Brownstein, K. R., and Tarr, C. E., *J. Magn. Reson.* **26,** 17 (1977).
39. Reyes, S. C., and Iglesia, E., *J. Catal.* **129,** 457 (1991).
40. Hollewand, M. P., and Gladden, L. F., *Chem. Eng. Sci.* **47,** 2757 (1992).
41. Lowell, S., and Shields, J. E., "Powder Surface Area and Porosity," 2nd ed. Chapman and Hall, London, 1984.